Applied Catalysis B: Environmental 334 (2023) 122861

Contents lists available at ScienceDirect

Applied Catalysis B: Environmental

journal homepage: www.elsevier.com/locate/apcatb

The in-situ formation of supported hydrous ruthenium oxide in aqueous phase during HDO of lignin-derived fractions

Evgeny Naranov [a,*], Alexey Sadovnikov [a], Olga Arapova [a], Tatiana Kuchinskaya [a], Oleg Usoltsev [b], Aram Bugaev [c], Kwinten Janssens [d], Dirk De Vos [d], Anton Maximov [a]

[a] Topchiev Institute of Petrochemical Synthesis, Russian Academy of Sciences, Leninsky prospekt, bld. 29, 119991, Moscow, Russia
[b] The Smart Materials Research Institute, Southern Federal University, Sladkova 178/24, 344090, Rostov-on-Don, Russia
[c] SuperXAS beamline, Paul Scherrer Institute, Forschungsstrasse 111, 5232 Villigen PSI, Switzerland
[d] Centre for Membrane Separations, Adsorption, Catalysis and Spectroscopy for Sustainable Solutions (cMACS), KU Leuven, Celestijnenlaan 200F, post box 2454, 3001 Leuven, Belgium

ARTICLE INFO

Keywords:
Bio-oil
Guaiacol
Hydrodeoxygenation
Zeolites
Hydrous ruthenium oxide
XANES

ABSTRACT

The in-situ formation of supported hydrous ruthenium oxide (HRO) from RuO_2 over micro-mesoporous materials is reported for the selective hydrogenation of bio-oil under mild reaction conditions (200 °C, 20 bar H_2) in an aqueous medium. For the first time, the phase composition of HRO was determined using a variety of characterization techniques. Using synchrotron radiation and in-situ X-ray absorption spectroscopy (XAS), we demonstrated that HRO was generated during the hydrodeoxygenation process. The hydrodeoxygenation (HDO) of real bio-oil was successfully performed at 200 °C, 20 bar H_2 on RuO_2-containing catalysts. The approximate composition of HRO after 3 h of catalytic hydrogenation, consisted of in approximately equal ratios metallic Ru, RuO_2, and RuOOH phases.

1. Introduction

Nowadays, one of the main trends in upgrading renewable feedstocks is focused on the hydrodeoxygenation (HDO) of lignin-derived substances into hydrocarbons or aromatics by the complete deoxygenation [1–11]. Selective hydrogenation of lignin-derived compounds to valuable products such as phenol, cyclohexanol and its alkyl derivatives is a promising process in green chemistry [12–15]. Those chemicals can be used in the production of plastics, paints, detergents and in many other applications [16]. HDO of bio-oil molecules requires a certain set of properties that the catalysts have to possess: high acidity, specific surface area and stability [9,10,16–18]. For instance, bio-oil fractions contain a number of high-molecular weight compounds, therefore, the diffusion limitations should be taken into account to prevent premature coke formation in the catalysts pore system. To avoid this issue, mesoporous zeolites have been applied in the bio-oil hydroconversion [19–22]. Almost all of the most common micro-mesoporous systems have been studied in this process: ZSM-5/MCM-41, ZSM-5/SBA-15, BEA/TUD, MWW/MCM-41, Ti-, Zr-containing materials and many others [10,23–28]. Among those micro-mesoporous structures, the nanosheets zeolitic materials attracted an increased attention due to their excellent catalytic performance in the acid catalyzed reactions [26,29–35]. Moreover, when bulky molecules are used as the substrate, such materials with an open structure, possessing active sites on the external surfaces, could catalyze the reactions without diffusional restrictions [21].

In general, biomass contains a lot of water (up to 50 wt%), as a consequence, fast pyrolysis of biomass often results in an aqueous bio-oil solution [2,6,36]. Being present in almost all biomass sources, water as a solvent should be considered for the HDO process [28,37]. There are a lot of studies reporting an HDO process in water using different heterogeneous and homogeneous catalysts. Some homogeneous catalytic systems such as Ni, Ru, V, Fe, Ni, RuNi are active in selective HDO process of aromatic oxygen contained substances under mild conditions [28]. There are a number of reports on active heterogeneous catalysts based on Ru, Re, Rh, Pd, and Pt [7,38,39]. These catalytic systems exhibit high activity in hydrogenolysis and hydrogenation reactions. Among these precious metals, ruthenium is oxophilic, highly active in HDO in the aqueous phase and least expensive [9,17,38,40–43]. The fact that Ru is active in water is due to the interaction of adsorbed water

* Corresponding author.
E-mail address: naranov@ips.ac.ru (E. Naranov).

https://doi.org/10.1016/j.apcatb.2023.122861
Received 14 February 2023; Received in revised form 14 April 2023; Accepted 6 May 2023
Available online 12 May 2023

molecules with substrate on the active sites through the hydrogen bonding [14,28,44]. Insyani and Tu found out that the interfacial RuO_2–Ru sites suppressed humin formation and resulted in higher hydrogenated products yields due to better adsorption of intermediates and substrate [45,46]. This observation initiated further studies where the hydrous form of ruthenium was compared to common anhydrous Ru catalysts. It was found that the hydrous form was more active compared to conventionally used ones, since the water molecules near the Ru species adsorb the substrate on their surface through hydrogen bonding followed by HDO [47].

However, there is a lack of information regarding the nature of Ru active sites in aqueous solutions. The structure of ruthenium hydrous oxides is still unknown as well as the reason of its high activity. There are studies pointing out that hydrous ruthenium oxide (HRO) is a simple oxide $RuO_2{\cdot}xH_2O$ [48]. Thallada and Kumar have stated that HRO consisted of Ru, RuO_2 and $Ru(OH)_3$ [14]. Gundekari and Srinivasan confirmed the presence of Ru in the spent catalyst during reduction of Ru(IV) and Ru(VI) species [47]. More physico-chemical data about the nature of such acid sites are of paramount importance for the development of effective HDO catalysts. In this work, the in-situ formation of ruthenium hydrous oxide supported on MFI nanosheets is reported. The evolution of the phase transformation ruthenium oxide (IV) → ruthenium hydrous oxide in aqueous solution during HDO process was thoroughly investigated. For the first time, in-situ X-ray absorption near edge structure (XANES) data under high pressure and temperature was collected during HDO process.

2. Experimental section

2.1. Materials synthesis

In this study three types of materials with different morphology was synthesized: (S1) 1D pore structure “MCM-41-like” mesoporous material with ZSM-5 crystallites, (S2) mixed phase of 1D pore structure “MCM-41-like” and MFI nanosheets and (S4) MFI nanosheets morphology. Typical double-templating procedures of S(X) (X – seed concentration ratio) were as follows: A – Seeding gel preparation, B – Micellar gel preparation, C – Crystallization.

(A) 0.69 g NaOH, 5.9 g tetrapropylammonium hydroxide (1 M) was dissolved in 35.5 g H_2O and mixed thoroughly. Then, 6.9 g fumed silica (SiO_2) was added in portions under stirring. The mixture was aged at 100 °C for 16 h.

(B) 43.3 g H_2O was used to dissolve 0.69 g NaOH and 4.4 g cetriltrimethylammonium bromide followed by a thoroughly mixing. Subsequently 0.36 g of $NaAlO_2$ was added along with 4.6 g fumed silica (SiO_2) (in portions under stirring). The mixture was aged at 100 °C for 16 h. The content of (A) equal to 1.75 g, 3.5 g, 7.0 g was added to the mixture (B) as a seeding gel, respectively for the materials denoted as for S1; S2; S4. The resulting gel was stirred for one hour.

(C) Crystallization was performed using a Teflon-lined stainless steel autoclave at 150 °C for 48 h.

Thereafter, the samples were washed with deionized water and dried at 95 °C for 12 h. Finally, the materials were calcined at 550 °C for 6 h to remove the remaining surfactant. Proton forms of the samples were prepared by ammonium nitrate exchange at 85 °C for 2 h (3 times) followed by drying at 95 °C overnight and calcination at 550 °C for 6 h. The loading of the metal (5.0 wt% Ru) onto these supports was done by incipient wetness impregnation using the solution of ruthenium chloride ($RuCl_3{\cdot}H_2O$, "Aurat", ω(Ru) ≥ 46.0 wt%) as the metal precursor. In a typical synthesis of Ru-containing catalysts, the calculated amount of ruthenium chloride was dissolved in water. Then, a porous material (calcined at 550 °C) was added to $RuCl_3$ solution under stirring and kept at room temperature overnight. The sample was dried at 90 °C for 12 h and then at 120 °C for 3 h followed by calcination at 400 °C for 5 h.

2.2. Catalytic experiments

Hydrogenation of oxygen-containing substances (guaiacol or bio-oil) was conducted in a steel autoclave equipped with a magnetic stirrer and a pressure gauge [49]. The autoclave was charged with 0.010 g of catalyst, 0.100 g of guaiacol or bio-oil and 0.5 mL of H_2O (inner volume of autoclave - 5 mL). The bio-oil was purchased from BTG (Netherlands), the detailed composition of bio-oil was showed in [50]. The autoclave was filled with hydrogen to a pressure of 20 bar. The reaction was run at 170–200 °C with a stirrer speed of 700 rpm. After the reaction, the autoclave was cooled to room temperature and the pressure was decreased to atmospheric pressure.

The qualitative composition of the liquid products was determined by gas chromatography - mass spectrometry (GC-MS) using a Finnigan MAT 95 XL instrument equipped with a Varian VF-5MS capillary column and helium as a carrier gas (1.5 cm^3/min). Temperature programming was conducted as follows: holding at 34 °C for 5 min, heating to 290 °C (10 °C/min), holding for 10 min. The concentrations of the products were calculated by the ratio between the corresponding peak area and the sum of the area of the peaks considering the response factors of pure substances. The results were processed using the Xcalibur software package. The products were identified by matching their mass spectra against the dedicated mass spectra library of the software.

NMR analysis was performed on bio-oil sample and products with each sample being dissolved in 2 mL of dimethyl sulphoxide-d6 (DMSO-d6). The ^1H and, ^{13}C NMR and HSQC spectra were recorded at 25 °C on a Bruker Avance III HD (400 MHz) NMR spectrometer (Rheinstetten, Germany) operating at a frequency of 400 MHz for ^1H and 100 MHz to detect the presence of ^{13}C. The ^1H spectra were recorded at 1024 scans and 0.2 s acquisition time. The ^{13}C spectra were recorded at 1024 scans and 0.01 s acquisition time. The central solvent peak (DMSO-d6) was used for calibration of the chemical shift. After catalytic experiments the products were dissolved in 2.2 g of DMSO-d6.

Structural features and changes of acid sites of Ru- catalysts and intermediates formed during hydrogenation of guaiacol were studied using in-situ high-temperature diffuse reflectance infrared Fourier transform (DRIFT) spectroscopy, which made it possible to measure the infrared (IR) spectra of zeolite catalysts at 200 °C in a dry hydrogen flow. The sample was placed in a PIKE Diffuse IR high-temperature cell coupled with a Bruker VERTEX-70 FTIR spectrometer. Spectra were taken in a continuous mode for 5 min (194 scans/spectrum) with a resolution of 2 cm^{-1} in the range of 4000–600 cm^{-1}. The Y axis in the spectra corresponds to the optical density ($D = \log(I_0/I)$). At first, the catalysts were heated up to 450 °C in an Ar atmosphere, then the temperature was decreased to 200 °C when the substrate and hydrogen flow was turned on. After that, the spectra were recorded for one hour. The reduced catalysts were activated after heating in Ar by switching to H_2 flow at 300 °C for one hour. Then the temperature was decreased to 200 °C and the substrate flow was introduced. Guaiacol was introduced to the catalytic system by hydrogen flow at a rate of 0.7 L/h.

2.3. Characterization

The textural characteristics of the samples were determined by low-temperature nitrogen adsorption (77 K) using a Micromeritics ASAP 2020 instrument. Prior to analysis, the samples were degassed at 350 °C for 6 h. The specific surface area was calculated by Brunauer-Emmett-Teller (BET) theory at a relative partial pressure of $P/P_0 = 0.2$; the pore size distribution was calculated according to the Barrett–Joyner–Halenda (BJH) model using adsorption data following the approach proposed by Ryoo and co-workers [51].

The composition of the samples was analyzed by atomic absorption spectrometry using a PerkinElmer Analyst instrument. X-ray powder diffraction analysis was carried out using a Rigaku D/MAX 2500 diffractometer (CuK_α radiation) in the 2Θ range of 1–50°, with a goniometer rotation speed of 1°min^{-1}. The X-ray phase analysis of the

samples after catalysis was carried out from the suspension without preliminary drying.

The XPS measurements were performed using a "PREVAC EA15" electron spectrometer. In the current work, AlKα ($h\nu = 1486.6$ eV, 150 W) were used as a primary radiation source. The pressure in analytical chamber did not exceed 5×10^{-9} mbar during spectra acquisition. The binding energy (BE) scale was pre-calibrated using the positions of $Ag3d_{5/2}$ (368.3 eV) and $Au4f_{7/2}$ (84.0 eV) from silver and gold foils, respectively. The powdered catalyst samples were supported onto double-sided conducting scotch tape. The spent catalyst suspended in the reaction products was transferred by pipettor to the holder of the XPS system in order exclude the air exposure. To take into account the effect of surface charging, the C1s at ($E_b = 284.8$ eV) from the carbon contamination was used as an internal standard.

Temperature-programmed reduction with hydrogen (TPR-H_2) was performed using AutoChem 2950HP instrument (Micromeritics Instrument Corp., Norcross, GA, USA). In a typical procedure, a sample was purged with Ar flow at 400 °C for 1 h, then cooled down to 50 °C. The reduction was performed under the 30 mL/min flow of 8 vol% H_2–92 vol % Ar mixture in the range of 50–400 °C with a ramp of 10 °C/min. Pulse chemisorption of CO was performed in a quartz reactor using AutoChem 2950HP (Micromeritics Instrument Corp.; Norcross, GA, USA). Samples were reduced with H_2 at 350 °C for 30 min, purged with He for 30 min, and cooled down to room temperature. A mixture of 3% CO + He (balance) was applied, loop volume was 0.5 mL. The calculations were performed by formulas described in the article [52]. TGA was performed on Mettler TA 4000 system. The heating and cooling of samples was performed at a rate of 10 °C/min under air flow of (70 mL/min) in the range from − 20–800 °C.

Raman spectra of catalysts were acquired in the range from 3700 to 100 cm^{-1} by using a Senterra II confocal Raman microscope (Bruker) using a 785 nm laser (1 mW) for catalyst samples before and after the reaction, and 532 nm laser (0.25 mW) for ruthenium oxide sample, and with the 50 × ocular. Acquisition time was 9 s, 25 scans were recorded and averaged for each sample. The experiments were performed at room temperature (RT) in air without any pretreatment.

Fourier transform infrared (FTIR) spectra were recorded on The Nicolet iS10 spectrometer. Prior to the measurements, the catalysts were pressed into self-supporting disks and activated in the IR cell attached to a vacuum line at 673 K for 2 h. Adsorption of pyridine was performed at 423 K for 20 min. Excess probe molecules were further evacuated at 423 K for 20 min. The numbers of Brønsted and Lewis acid sites were determined from the intensities of the bands at ca. 1545 and 1455 cm^{-1} of adsorbed pyridine, respectively, using the molar extinction coefficients given by Tamura et al. [53].

For transmission electron microscopy (TEM) FEI's Tecnai Osiris TEM with an accelerating voltage of 200 keV was used. Scanning electron microscopy (SEM) images and energy-dispersive X-ray (EDX) spectra were recorded using an NVision 40 microscope (Carl Zeiss) equipped with the X-Max 80 EDX detector (Oxford Instruments).

Density functional theory (DFT) calculations were proceeded in VASP [54–56]. The plane wave basis set with cut off energy of 500 eV was selected. Monkhorst-pack algorithm was used with 5×5x1 grid in reciprocal space. The unit cells consisted of 48 Ru atoms (3 layers) for Ru (111) surface, 32 Ru and 48 O atoms for RuO_2 (110) surface and 12 Ru, 24 O and 14 H atoms for RuOOH (001) surface. Relaxations of guaiacol molecules on the surfaces were carried out keeping the surface atoms fixed. Bonding energies were calculated as difference between optimized molecule on the surface and a sum of the energies of the molecule in vacuum and pure surface.

2.4. In-situ XANES studies

To examine the phase transformation of Ru species during guaiacol hydrogenation in water an in-situ XANES experiment was performed. A special home-made autoclave-type in-situ cell was designed to collect the data in transmission mode [49]. Two collinear holes were made in the cell body to allow the X-ray beam passing through the sample. The cell was equipped with Teflon reaction vessel which was placed in aluminum tube (0.5 mm thick) to prevent the Teflon body from thermal and high-pressure expansion through the X-ray holes. The temperature was regulated by four 50 W heaters and was controlled by a type K thermocouple attached to the channel in the cell body. The working volume of a Teflon vessel was 5.3 mL.

In-situ XANES spectra were collected at BM23 beamline of ESRF. The energy was selected by a Si(311) double-crystal monochromator operated in the continuous scanning mode. Higher harmonics were rejected by Rh-coated mirrors. The beam intensity before and after the cell were measured by ionization chambers. Ru foil was measured simultaneously with the samples for energy calibration. Data processing and analysis were performed in a self-written Python code using pyFitIt [57], pyMCR [58], and Larch [59] libraries.

3. Results and discussion

3.1. The structure analysis

We developed three types of micro-mesoporous materials with different morphology: (S1) "MCM-41-like" mesoporous material with ZSM-5 crystallites, (S2) mixed phase of "MCM-41-like" mesoporous material and MFI nanosheets and (S4) MFI nanosheets [60]. At first, the supported RuO_2 catalytic systems were synthesized. The textural characteristics are presented in Table 1.

Pristine S1, S2 and S4 materials exhibited IV^{th} curve (IUPAC) with a slight shift towards I type (typical for microporous materials) [60]. Textural characteristics of the synthesized catalysts in the oxide form are presented in Table 1. These results suggest that the introduction of RuO_2 in the pore structure did not affect the microstructure at a significant level. The BET surface area of the RuO_2/S1, S2 and S4 catalysts were lower than those of the pristine S1, S2 and S4 micro-mesoporous supports. RuO_2 particles that were distributed inside the pore system, could block some of the mesopores, resulting in a decrease in the surface area.

The morphology of the RuO_2-catalysts was investigated using SEM and TEM (Fig. 1). Fig. 1b shows that the RuO_2/S1 sample represents the MCM-41-like mesoporous ordered structure containing RuO_2 particles. For RuO_2/S4, nanosheets morphology was revealed containing pretty much the same size and shape RuO_2 particles. The RuO_2/S2 catalyst possesses an intermediate morphology between MFI nanosheets and MCM-41-like (Fig. 1a and b). The particle size of RuO_2 according to TEM in all three samples was relatively large – up to 25 nm. The exact values were determined by CO pulse chemisorption. The results were displayed in Table 1.

3.2. RuO_2 phase characterization

The phase analysis of the Ru-supported catalysts was performed

Table 1
Characteristic of supports and RuO_2 catalysts.

Sample	Si/Al (a)	S_{BET}, m^2/g (b)	V_{micro}, cm^3/g	V_{meso}, cm^3/g	V_{total}, cm^3/g	Particles size, nm (c)	Ru content, wt% (a)
S1	21	1100	0.05	0.80	0.85	-	-
S2	20	650	0.08	0.42	0.50	-	-
S4	23	510	0.10	0.25	0.35	-	-
RuO_2/S1	21	1060	0.05	0.74	0.79	25	4.8
RuO_2/S2	21	600	0.07	0.43	0.50	23	5.2
RuO_2/S4	23	500	0.10	0.22	0.32	26	4.9

(a) ICP/OES analysis. (b) BET specific surface area from adsorption isotherm in the relative pressure range 0.05–0.20. (c) by CO chemisorption

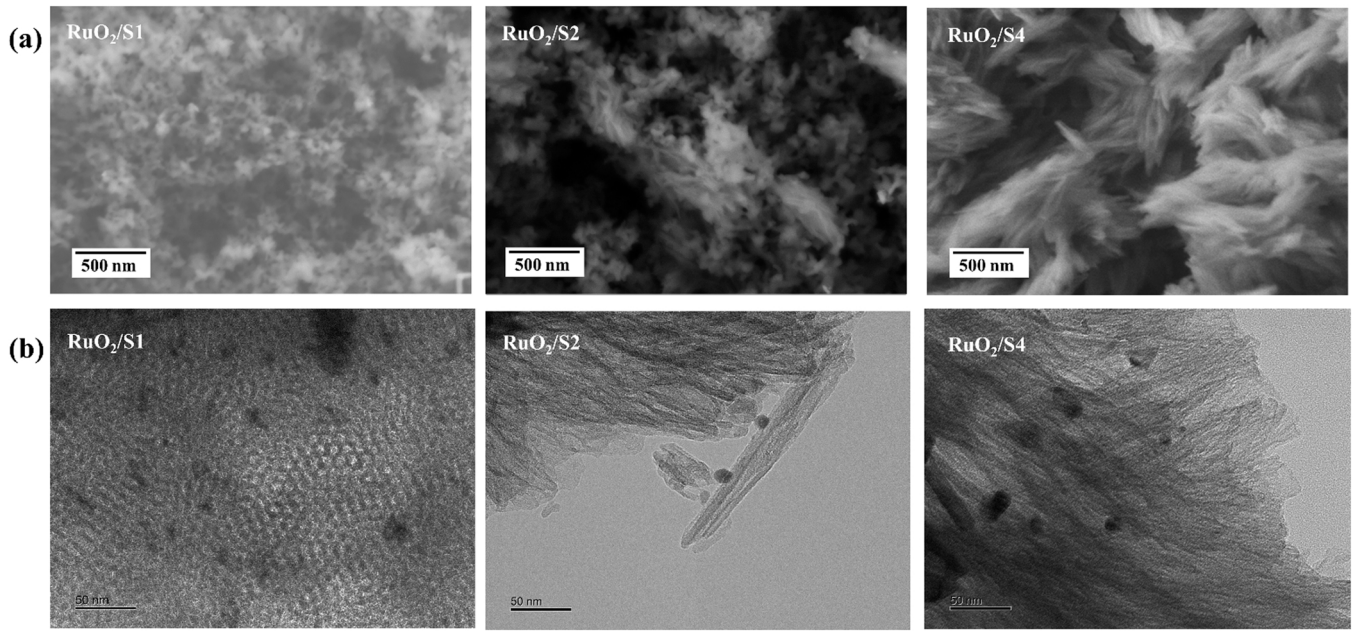

Fig. 1. (a) SEM and (b) TEM images of RuO_2 catalysts.

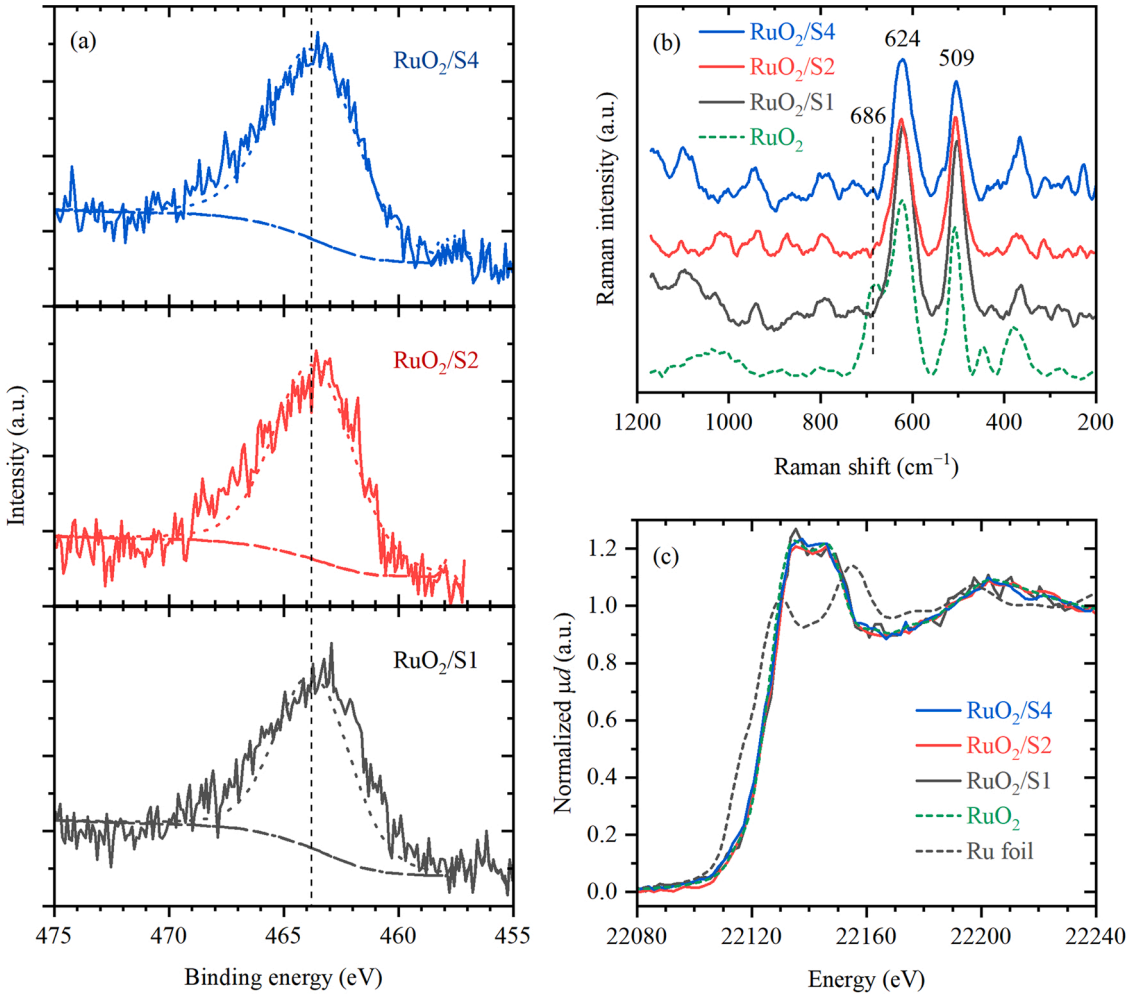

Fig. 2. (A) X-ray photoelectron spectroscopy (XPS) spectra of Ru $3p_{3/2}$ for RuO_2/S1-S4, (B) Raman spectra and (C) XANES spectra of RuO_2 catalysts compared to RuO_2 (dashed green line) and Ru foil references (dashed grey line).

using XRD, and the results are presented in Fig. S2c. The reflections at 2θ of 28°, 35° and 54° correspond to the (100), (002), and (101) planes, respectively, of RuO_2 phase (JCPDS # 65–2884). The electronic states of ruthenium contained catalysts were analysed by XPS, and the spectra are presented in Fig. S2a, S2b, and Fig. 2a. The XPS spectra were referenced to the main C 1 *s* peak at 284.8 eV. The main signals at 463.7 eV in the Ru $3p_{3/2}$ XPS spectrum (Fig. 2a) corresponded to Ru^{4+}. The signal at 461.7 eV corresponding to Ru^0 was not detected. The Ru $3d_{5/2}$ XPS spectra of the RuO_2 catalysts are presented in Fig. S2b. The peak at 282.2 eV in the Ru $3d_{5/2}$ XPS profiles of the catalysts further confirmed the presence of Ru^{4+} [45]. The peak at 279.9 eV in the Ru $3d_{5/2}$ XPS profiles of the catalysts belonging to the metallic Ru^0 phase were not detected. The similar XPS spectra of Ru in each sample suggested that the synthesis procedure allowed to obtain the same initial RuO_2 nanoparticles over a support of a different type.

To ascertain once again the RuO_2 –catalysts nature, Raman spectroscopy was carried out (Fig. 2b). The major Raman active modes for RuO_2 are E_g at 509 cm^{-1}, $A_{1\,g}$ at 624 cm^{-1} and $B_{2\,g}$ at 687 cm^{-1}. It should be noted that the three Raman modes of single crystal of ruthenium oxide are located at 523, 645, and 710 cm^{-1} [61]. Synthesized RuO_2 catalysts showed a red-shift of about 20 cm^{-1}, what can be attributed to the nanosized RuO_2 species [62].

The chemical environments of Ru species were examined by Ru *K*-edge XANES (Fig. 2c). XANES spectra of all three samples were identical to that of RuO_2 reference confirming the Ru(IV) state in the as-prepared catalysts.

The reduction properties of RuO_2 catalysts were analysed by H_2-TPR. Fig. S3 shows that the position of the TPR curves maxima poorly depends on the supports. The peak position was located at 120 – 127 °C (126.5 °C for RuO_2/S1, 125 °C RuO_2/S2 and 120 °C for RuO_2/S4). Since the S4 material consisted of nanosheets, the RuO_2 nanoparticles were located between the zeolite layers which are easy to penetrate than 1D (MCM-41-like) mesoporous structure. However, there are many studies interpreting the difference in the dependences of H_2-TPR on the supports acidity and its strong metal-support interaction [46,63]. Generally, when there is no strong metal-support interaction the H_2-TPR profiles represent single peak in the 140–170 °C [64,65]. The acidity of the supports and Ru-catalysts was studied using pyridine FT-IR. The types and concentrations of the acid sites of RuO_2/SX (X – 1, 2, 4) catalysts are presented in Table 2. The acidity of micro-mesoporous materials slightly changed after the introduction of RuO_2. There was a decrease of Lewis acid sites in all catalysts. It is known that the changes in the acid site concentration could be expected due to interactions between RuO_2 nanoparticles and acid sites. Since RuO_2 particles size is greater than MFI pores, it leads to the catalyst distribution at the outer surface of the zeolite structure. Therefore, a majority of the particles would not interact with acid sites.

3.3. Guaiacol hydroconversion

Since the materials morphology was quite different (unlike the initial state of RuO_2 particles), the dependence of catalytic activity on materials characteristics was accurately compared, using guaiacol as a model substrate. Ru zeolite catalysts have been widely studied as an HDO catalysts due to their high activity in the HYD (hydrogenation) and HDO of guaiacol [9,10,44,66–68]. Hydrogenation of guaiacol over Ru-contained acidic catalyst can occur via HYD/HDO or HYD reaction pathways (Scheme 1). At first, fully hydrogenated product 2-methoxycyclohexanol is formed. Then, depending on the catalysts acidity and reaction conditions HDO can occur. In some cases direct deoxygenation can happen [18,43]. When the substrate is directly deoxygenated, oxygen is usually removed without aromatic ring saturation. In that scenario phenol can be produced. After full hydrogenation, guaiacol is saturated to obtain 2-methoxycyclohexanol, followed by sequential deoxygenation to produce cyclohexanol and cyclohexane (in some cases methoxycyclohexane).

Table 2
Acidity of micro-mesoporous materials measured by FTIR spectroscopy of adsorbed pyridine, μmole/g.

Sample	BAS [(a)]	LAS [(a)]	BAS/LAS [(b)]
S1	44	146	0.30
S2	54	126	0.43
S4	72	88	0.81
RuO_2/S1	47	113	0.42
RuO_2/S2	52	98	0.53
RuO_2/S4	80	80	1

(a) acidity from FTIR of adsorbed pyridine analysis, (b) ratio of Brønsted acid sites to Lewis acid sites,

The hydroconversion of guaiacol in water was conducted under mild conditions at 170 – 200 °C and 20 bar of H_2. 2-Methoxycyclohexanol was obtained as the major product, while trace amounts of phenol (<0.2%) and relatively small amounts of cyclohexane were also detected in the product mixture (Table 3). Moreover, negligible amounts of aromatic products, resulting from the DDO (direct deoxygenation) pathway such as anisole and benzene, were obtained in the product mixture. Since the reaction was conducted at relatively low temperatures (up to 200 °C), the HYD route was highly preferred over DDO [41,69]. From the thermodynamic point of view, hydrogenation of aromatics is more advantageous way than the oxygen removal under the studied conditions [70], therefore, the phenol formation is negligible due to the fact that phenol was the intermediate of cyclohexanol formation [71]. The bond strength of C(Ar)-O is more than 80 kJ/mole greater than C(sp^3)-O, which implies that the HDO would be easier via hydrogenation step first [72], however in the case of acidic catalysts, the dehydration step can occur [73]. The in-situ DRIFT analysis of guaiacol hydrogenation over RuO_2 catalysts demonstrated the demethoxylation/demethylation step increased in the following order RuO_2/S1 < RuO_2/S1 < RuO_2/S1 (by the intensity of phenol formation, Fig. S8-9). Nevertheless, the benzene ring saturation was dominant in all catalytic system.

The turnover frequency – TOF for the series of catalysts were calculated based on the assumption of exposed Ru sites being only active site for guaiacol hydrogenation. The number of exposed Ru sites in each catalyst were determined by CO chemisorption. TOF(h^{-1}) was calculated by dividing moles of converted guaiacol within 0.25 h of the reaction (mol/h) by the number of exposed Ru sites (mol). Under these conditions the conversion of guaiacol did not exceed 50 wt%. Apparent activation energy (E_a) was determined from the Arrhenius plot by conducting the hydrogenation process at different temperatures (Fig. 3). For RuO_2/S1 and RuO_2/S2, the apparent E_a were 45 and 48 kJ/mol respectively. For RuO_2/S4 E_a decreased to 28 kJ/mol suggesting the difference in the availability of active sites. Since the size effect of the RuO_2 nanoparticles could not be related to activity due to the similarity of nanoparticles nature and shape, the decrease in the apparent activation energy could be induced by the difference in the supports' morphology and acidity. A series of experiments was conducted at 200 °C, 20 bar H_2 for 0.25 h using different stirring rate, ranging from 300 to 1000 rpm for each catalysts. The activity of the catalysts remained the same, therefore, the external mass transfer limitations could be neglected.

The products distribution was determined at different reaction time. Guaiacol was partially converted (ca. ~50%) to hydrogenated products after 15 min of conducting experiment. The time needed to achieve the complete conversion of guaiacol at 200 °C was longer than 3 h. At the beginning of reaction, a high selectivity towards 2-methoxycyclohexanol was observed (> 50%), after that it was converted to HDO products such as cyclohexanol and cyclohexane (for RuO_2/S2 and RuO_2/S4). The content of HDO products was clearly dependant on the BAS concentration, e.g. the selectivity towards cyclohexane was in the following order: RuO_2/S1 < RuO_2/S2 < RuO_2/S4. The difference in selectivity towards cyclohexane was much greater than the difference in the BAS

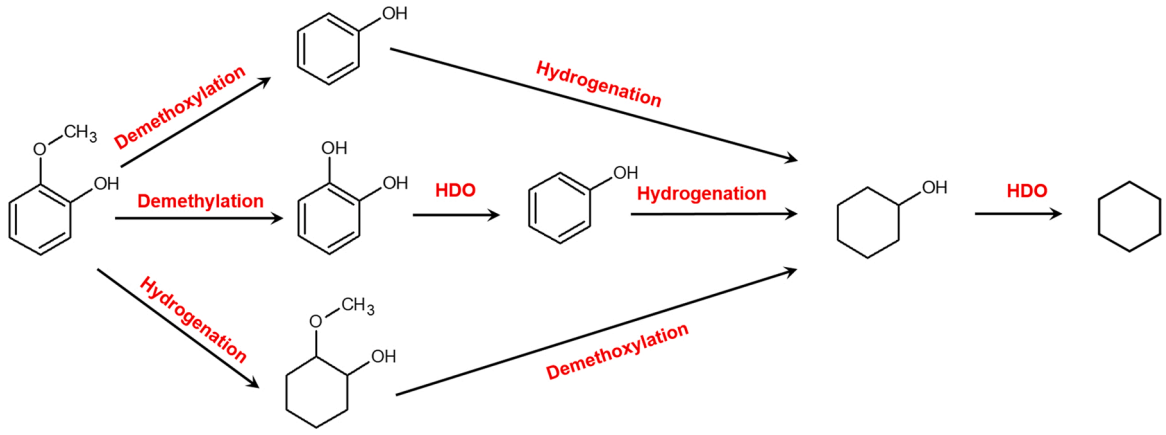

Scheme 1. General reaction pathways of guaiacol hydrogenation.

Table 3
Selectivity over different catalysts. Reaction conditions: 200 °C, 20 bar H_2, catalysts mass 0.05 g.

0.25 h	RuO_2/S1	RuO_2/S2	RuO_2/S4
Conversion, %	55	62	62
2-methoxycyclohexanol	56	55	51
cyclohexanol	44	45	47
cyclohexane	0	0	2
0.5 h			
Conversion, %	78	81	85
2-methoxycyclohexanol	43	50	41
cyclohexanol	57	50	55
cyclohexane	0	0	4
1 h			
Conversion, %	85	85	91
2-methoxycyclohexanol	38	45	30
cyclohexanol	62	53	60
cyclohexane	0	2	10
3 h			
Conversion, %	89	91	95
2-methoxycyclohexanol	31	44	23
cyclohexanol	68	51	61
cyclohexane	1	5	16

concentration (Table 2). Therefore, it was suggested that the availability of Ru-species located near BAS could affect catalysis. MFI nanosheets possess the highest external strong acid sites sites compared to different porous materials [29]. In this regard, the possibility of Ru-species location around the BAS is much higher in the case of S4 material than S2 and especially S1 material with cylindrical pores. The performance of RuO_2/S4 in the guaiacol hydrogenation was compared with various catalytic systems based on Ru (Table S2). Under similar conditions, the application of Ru catalyst in the oxide phase supported on MFI nanosheets turned out to be beneficial.

The recyclability of Ru-containing catalysts was tested at 200 °C in 3 catalytic runs. Before the next hydrogenation reaction, the spent catalyst was thoroughly washed with acetone and dried at 95 °C for 3 h and calcined at 400 °C in order to oxidize any reduced Ru species. It was shown that the conversion of guaiacol was maintained, the catalysts kept their initial activity.

To establish the reaction intermediates and products, the hydrogenation of guaiacol, HDO process, was studied by in-situ high-temperature DRIFT method. In order to compare the difference between the oxidized and reduced Ru catalysts, all catalysts were studied in both forms. Fig. 4 shows the differential surface spectra of the catalyst based on material S1, i.e. the spectrum of the pure catalyst recorded at the same temperature was subtracted from the surface spectrum of the catalyst with the substrate. According to the literature data [74], in the

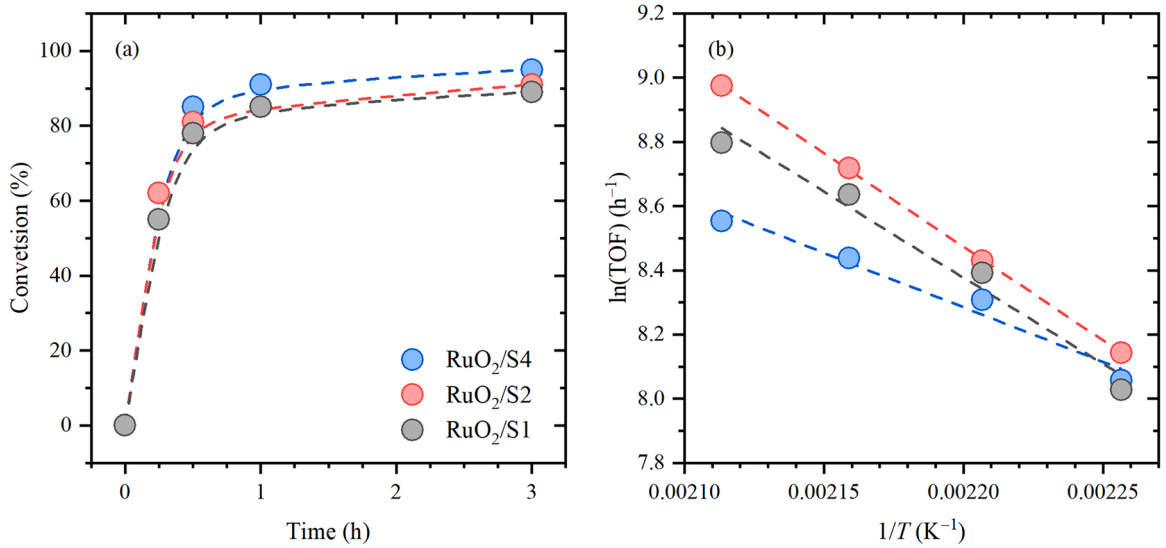

Fig. 3. Comparison of micro-mesoporous catalysts activity: **(a)** Kinetic analysis of guaiacol hydrogenation at 200 °C, 20 bar H_2, **(b)** Arrhenius plots for the guaiacol hydrogenation (reaction conditions: 20 bar H_2, 0.25 h).

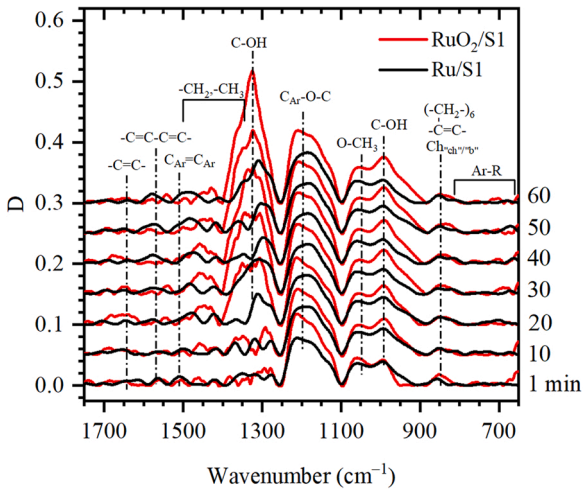

Fig. 4. Differential DRIFT spectra of RuO_2/S1 and reduced Ru/S1 catalyst surface under a substrate and hydrogen flow during 1 h.

IR spectra of aromatic and aliphatic ethers and alcohols, the most intense bands of stretching mode of C_{Ar}-O(νC_{Ar}.O) bonds are located in the region of 1230–50 cm^{-1}, Alk-O ($\nu_{CH3\text{-}O}$) in the region of 1050 cm^{-1}, and C-OH bonds ($\nu_{C\text{-}OH}$) in the region of 970 cm^{-1}. This series of bands was well identified in the surface spectra of the RuO_2/S1 and Ru/S1 catalysts, apparently due to low concentration of BAS of the support. The band intensities at the beginning of the process were pretty similar over RuO_2/S1 and Ru/S1 catalysts. After 20 min of the experiment, a wide intense band at 1350–25 cm^{-1}, which is characteristic of secondary alcohols ($\nu_{C\text{-}OH}$) [73,75], including cyclohexanol, appears in the spectrum of the RuO_2/S1 surface. At the same time the band at 1400–1450 cm^{-1} from bending modes of CH_2 and CH_3 groups increases. In the DRIFT spectrum of the Ru/S1 surface, the intensity of the band at 1350 cm^{-1} is noticeably lower. After 20 min of experiments the bands at 970 cm^{-1} (C-OH) and 1050 cm^{-1} (O-CH_3) [7,39] became more intensive, indicating the formation of hydrogenated products. The RuO_2/S1 catalyst was more active than reduced Ru/S1. The observed phenomenon remained the same throughout the whole experiment, which clearly suggested that adsorption of the substrate and products was preferable in the case of RuO_2/S1 catalyst. For RuO_2/S2 and especially for RuO_2/S4 catalysts the results were less discernible due to the higher content of acid sites which can be adsorption centers for oxygen containing substances. However, the common trend of more active RuO_2 state was observed in more intensive bands for the formation of hydrogenated products (Fig. S8-S9).

3.4. Hydroconversion of bio-oil

The HDO of bio-oil obtained from hardwood products via rapid pyrolysis was performed at 200 °C and 2 MPa of H_2 in water for 3 h in an autoclave. This reaction led to a complex mixture which was mixed with DMSO-d_6 to homogenize products. The composition of bio-oil can be resolved by the application of 2D HSQC NMR analysis [76–78]. The results are shown in Fig. 5. The differences in signals density and distribution on 2D NMR spectra showed that upon hydroconversion the unsaturated functionalities such as alkenes, arenes and different ethers decreased while aliphatic and saturated ethers appear as dominating groups. As in the case of guaiacol hydrogenation, the RuO_2/S4 catalyst possessed the highest activity towards fully saturated products. R. Insyani et al. demonstrated that during HDO of oxygen-contained substances the presence of RuO_2 in Ru-catalyst suppressed the formation of humin and coke and favored the target products [45].

To analyze coke formation, the differential TGA of the spent catalysts was performed. The samples after catalytic experiments were dried at 80 °C for 6 h to remove water and light organic molecules. The results are shown in Table 4. The TGA analysis of spent catalysts confirmed the following order of the carbonaceous deposits content in the samples: RuO_2/S4 < RuO_2/S2 < RuO_2/S1. Therefore, we can conclude that an open structure such as nanosheets-like can prevent the catalytic system from excessive coke formation.

Since the initial bio-oil contained carboxylic acids, alcohols and other oxygen-containing molecules, the high content of acid sites could indeed lead to the side products. In order to compare the catalytic performance of reduced and oxidized catalysts, an additional experiment was conducted with bio-oil hydrogenation over reduced Ru/S4 catalysts. The results showed that in the case of Ru/S4 the content of residue after the catalytic process was higher compared with RuO_2/S4 catalyst. Therefore, we can conclude that RuO_2 interface played an important role in the HDO of oxygen contained substances by suppressing heavy products formation.

A number of additional analyses were used to elucidate the transformation of the Ru-phase after the HDO of bio-oil (Fig. 6b, c). The XRD analysis showed no characteristic metallic Ru reflexes in three spent catalysts, which could be attributed to the incomplete reduction or the small size of Ru nanoparticles (Fig. 6b, c). It was also demonstrated that the reflexes ascribed to (110) and (101) planes of RuO_2 structure got less intensive and dislocated to a new direction. The (110) reflex shifted to the lower angle direction, while the (101) reflex shifted to the opposite side. Furukawa et al. described this phenomenon during the electrochemical reduction of RuO_2 species as the partial reduction of ruthenium oxide to RuOOH [79]. Moreover, a simultaneous formation of amorphous phase (10–20°) was observed. The appearance of an amorphous phase could be due to carbonaceous deposits in the pore system.

The state of Ru in the spent catalysts as it was mentioned earlier is an open question. In a hydrocarbon solution the reduction of RuO_2 to metallic state occurs pretty fast [80]. With the presence of water, which contributes to the HDO process, the reduction slows down. Even after 3 h of hydrogenation, the final state was only slightly metallic. The XPS analysis of the spent catalysts revealed the partial presence of metallic Ru (Fig. 6a). However, the most abundantly observed Ru-phase was still an oxidized form. In Ru_{3p} XPS of hydrous ruthenium oxide (HRO)/S4, additional peaks appear at 463.4 and 466.8 eV belonged to the transformed RuO_2 to RuOOH and $RuO_2{\cdot}H_2O$. The signal attributed to RuOOH in the spent catalyst was negatively shifted by ~0.6 eV which also confirmed that Ru was in the hydrous form. Raman spectroscopic measurements were performed on the spent catalysts as shown in Fig. 6d. The spectrum of the catalysts shows a broad peak at 200–500 cm^{-1} which has been assigned to hydrated form RuO_2 [61]. The crystalline phase of any Ru-contained species was not detected.

The physicochemical analysis of the spent catalysts allowed us to assume an approximate composition of supported ruthenium hydrous oxide. Since the active sites in hydrogenation are supposed to be metallic ruthenium species and the XPS analysis confirmed their existence, the presence of metallic Ru is suggested. The diffraction patterns do not contain reflections of Ru which can be explained by the small size and amorphous nature. The RuO_x phase is inhomogeneous, which can be explained by the presence of Ru(III) and Ru(IV). According to XPS no phase is dominant, the composition of HRO can be described as miscellaneous.

To study the reason for higher activity of oxidized catalyst, the adsorption energies of guaiacol on the Ru(111), RuO_2(110) and RuOOH (001) surfaces were calculated at DFT level of theory. The most favourable adsorption positions and corresponding adsorption energies are presented in Fig. 7a-f. The binding energies of oxygen-containing substances on the Ru metallic surface are in agreement with the literature [41,81]. The obtained results showed that the surface of RuOOH was more prone to the adsorption of guaiacol. These results can be explained by assuming that hydroxyl groups on the RuOOH surface form donor-acceptor interactions with the substrate, e.g. the guaiacol adsorption in a flat geometry (Fig. 7c) is less favorable than the

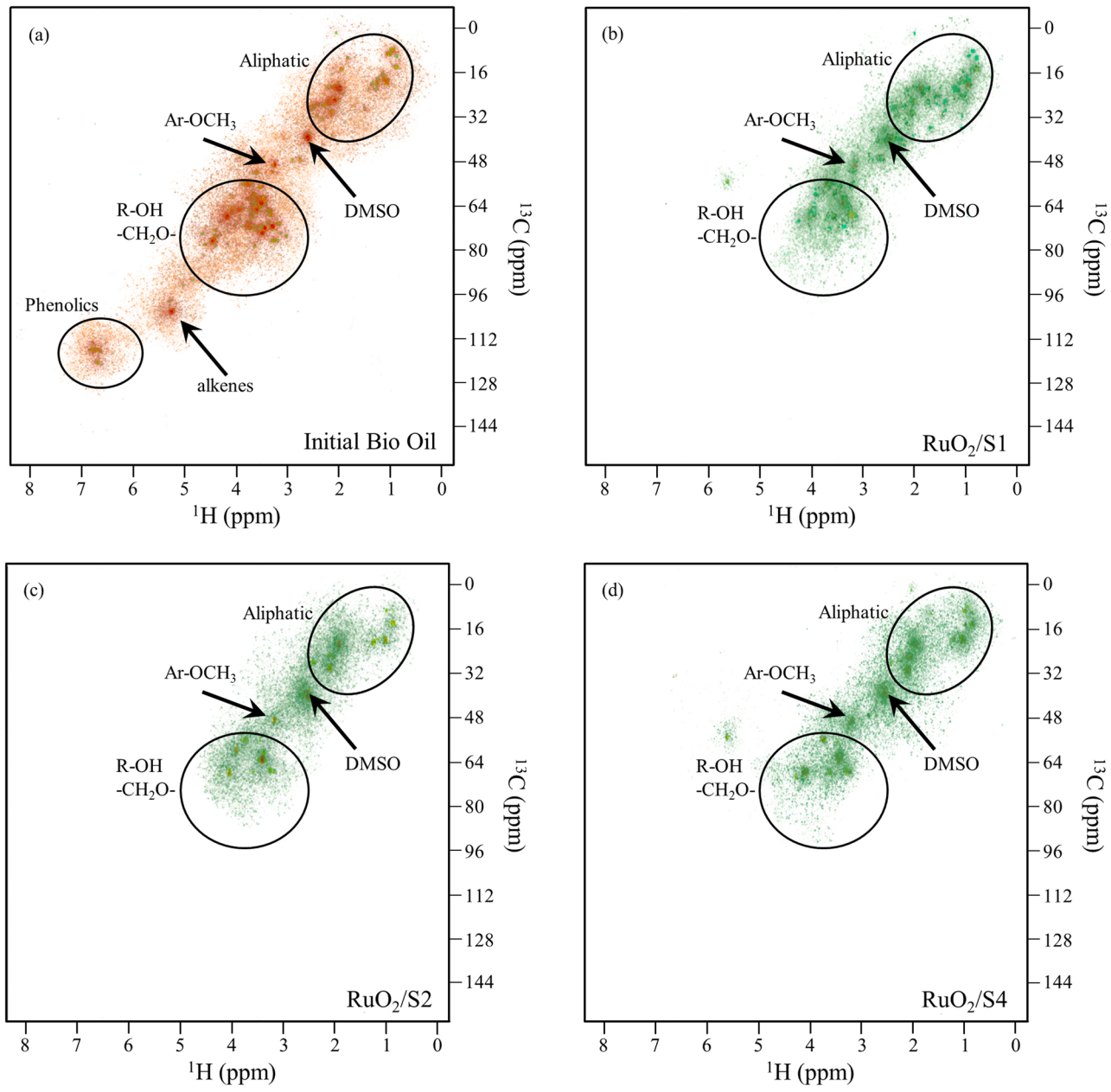

Fig. 5. 2D 1 H-13 C HSQC NMR spectra of initial and hydrogenated bio-oil over different catalysts at 200 °C, 20 bar H_2, 3 h.

Table 4
The content heavy residue in the synthesized catalysts after bio-oil hydrogenation by TGA analysis.

Catalysts	Heavy residue content, wt%
RuO_2/S1	16.1
RuO_2/S2	12.5
RuO_2/S4	8.7
Ru/S4	9.1

adsorption of an inclined hydroxyl group and –OCH_3 group (Fig. 7f) which was indirectly confirmed by in-situ high-temperature DRIFT results. These findings are in accordance with the study reporting that the presence of oxygen on the surface significantly favored adsorption geometries and energies [45]. To examine formation of active ruthenium sites during hydrogenation an in-situ XAS experiment was performed.

3.5. *In-situ evolution of Ru-species under high pressures and temperatures*

Ru *K*-edge XANES spectra of the Ru-based heterogeneous catalytic system were collected using the high-pressure cell schematically shown in Fig. S1. The catalytic system consisted of Ru catalyst dispersed in the water-guaiacol mixture and sealed under 20 bar of H_2 with continuous stirring. Upon the heating, we observed a shift of the absorption edge to lower energies for every sample, which indicated the reduction of the initial Ru(IV) oxide phase (Fig. 8). According to the position of the absorption edge indicative for the oxidate state, ruthenium is reduced from ca. 4 + to ca. 2 + (see evolution in Fig. S4). The spectrum of the resulting Ru(II) state does not possess isosbestic points with the reference spectra of RuO_2 (which is identical to the initial states of the catalyst) and ruthenium foil (Fig. S5a), thus, it cannot be represented as a linear combination of the known Ru(IV) and Ru(0) states (Fig. S5c). The formation of new type of Ru-species was also confirmed by the principal component analysis (PCA) of the whole XANES dataset (Fig. S6), which revealed the presence of three different Ru-species, two

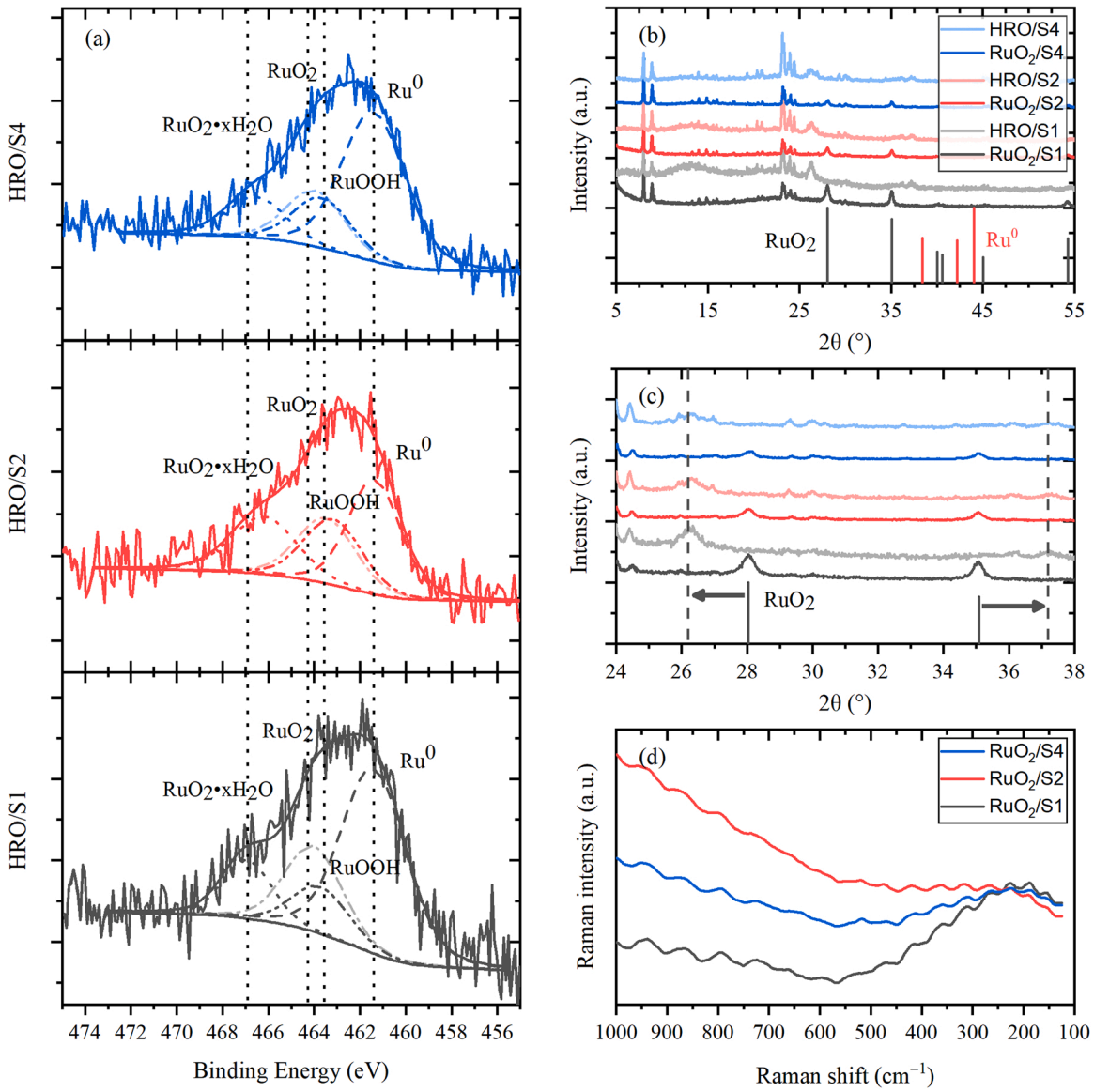

Fig. 6. (a) XPS spectra of Ru $3p_{3/2}$ for HRO/S1-S4, (b) XRD patterns in the 2θ range of 5–55°, (c) XRD patterns in the 2θ range of 25–37° and (d) Raman spectra of the catalysts after bio-oil hydrogenation.

of which were identified as Ru(IV) oxide and metallic Ru. Since the third species did not correspond to any of the available Ru reference spectra, an extensive screening of possible structures was performed by direct comparison of the experimental XANES spectrum with theoretically calculated ones. The best agreement (Fig. S5d) was observed for a structure of RuOOH shown in Fig. S7. Linear combination fitting (LCF) performed using theoretical spectra for RuO_2, metallic Ru, and RuOOH structures, revealed the coexistence of all three phases in the active catalyst (at the end of the heating). The phase fractions obtained from LCF are reported in Table S1.

4. Conclusion

In summary, we revealed the composition of ruthenium hydrous oxide supported on micro-mesoporous materials formed during hydroconversion of oxygen containing substances in aqueous media. *In-situ* XANES measurements allowed us to determine phase evolution of Ru-contained catalysts. It was found that the most active catalyst was hydrous ruthenium oxide HRO/S4 (that was formed from RuO_2/S4 during HDO) consisted of metallic Ru, RuO_2 and RuOOH. The in-situ DRIFT experiments showed preferential adsorption of guaiacol during hydrogenation on oxidized Ru species rather than reduced ones. It was demonstrated that morphology and acidity of the catalysts affected the product distribution in HDO: high content of acid sites leads to the production of deoxygenated products, while the structure of the support prevents coke formation. The obtained results suggest an efficient approach for the production of valuable chemicals from real bio-oils, and open new approaches for established bio refineries.

CRediT authorship contribution statement

Evgeny Naranov: Supervision, Project administration, Conceptualization, Investigation, Methodology, Writing – review & editing, Writing – original draft. **Alexey Sadovnikov:** Visualization, Investigation. **Olga Arapova:** Investigation, Formal analysis. **Tatiana Kuchinskaya:** Investigation. **Oleg Usoltsev:** Formal analysis, Visualization, Writing – review & editing. **Aram Bugaev:** Investigation, Writing – review & editing. **Kwinten Janssens:** Investigation, Writing – review & editing. **Dirk De Vos:** Writing – review & editing. **Anton Maximov:** Conceptualization.

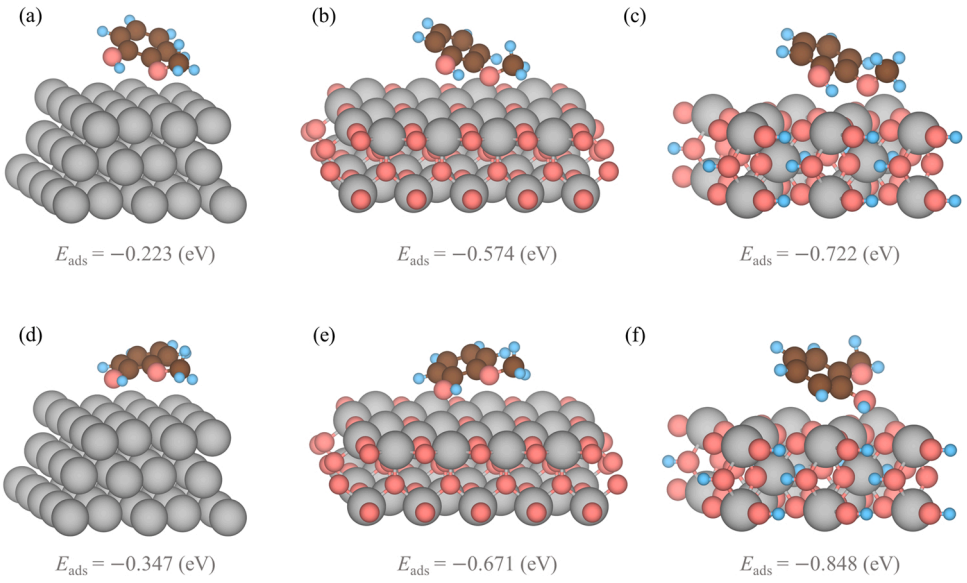

Fig. 7. Binding energies of guaiacol on the surfaces of Ru (a, d), RuO_2 (b, e), and RuOOH (c, f).

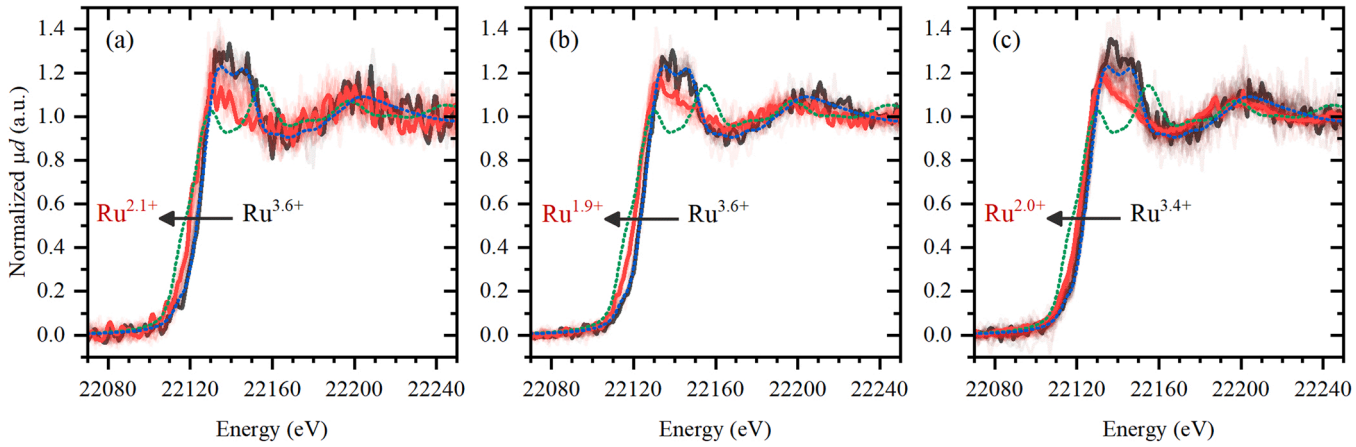

Fig. 8. *In-situ* XANES data (from black to red) during guaiacol hydrogenation over RuO_2/S1 (a), RuO_2/S2 (b) and RuO_2/S4 (c) compared to RuO_2 (dashed blue line) and Ru foil references (dashed green line). Reaction conditions: 200 °C, 20 bar H_2, 700 rpm.

Declaration of Competing Interest

The authors declare that they have no known competing financial interests or personal relationships that could have appeared to influence the work reported in this paper.

Data Availability

The authors are unable or have chosen not to specify which data has been used.

Acknowledgment

The authors from Topchiev Institute and Southern Federal University acknowledge the Ministry of Science and Higher Education of the Russian Federation for financial support (Agreement no. 075–15-2021–1363).

Notes

The authors declare no competing financial interest. The authors thank A.V. Shubnikov Institute of Crystallography RAS for TEM analysis, Dr. A.P. Glotov for his help to low-temperature adsorption-desorption of N_2 measurements. The SEM analysis was performed using the equipment of the JRC PMR IGIC RAS.

Appendix A. Supporting information

Supplementary data associated with this article can be found in the online version at doi:10.1016/j.apcatb.2023.122861.

References

[1] T.P. Vispute, H. Zhang, A. Sanna, R. Xiao, G.W. Huber, Renewable chemical commodity feedstocks from integrated catalytic processing of pyrolysis oils, Science 330 (80) (2010) 1222–1227, https://doi.org/10.1126/science.1194218.
[2] S. Xiu, A. Shahbazi, Bio-oil production and upgrading research: a review, Renew. Sustain. Energy Rev. 16 (2012) 4406–4414, https://doi.org/10.1016/j.rser.2012.04.028.
[3] A.V. Vutolkina, I.G. Baigildin, A.P. Glotov, A.A. Pimerzin, A.V. Akopyan, A. L. Maximov, E.A. Karakhanov, Hydrodeoxygenation of guaiacol via in situ H2 generated through a water gas shift reaction over dispersed NiMoS catalysts from oil-soluble precursors: tuning the selectivity towards cyclohexene, Appl. Catal. B Environ. 312 (2022), 121403, https://doi.org/10.1016/j.apcatb.2022.121403.
[4] P.M. Mortensen, J.D. Grunwaldt, P.A. Jensen, K.G. Knudsen, A.D. Jensen, A review of catalytic upgrading of bio-oil to engine fuels, Appl. Catal. A Gen. 407 (2011) 1–19, https://doi.org/10.1016/j.apcata.2011.08.046.

[5] S. Hansen, A. Mirkouei, L.A. Diaz, A comprehensive state-of-technology review for upgrading bio-oil to renewable or blended hydrocarbon fuels, Renew. Sustain. Energy Rev. 118 (2020), 109548, https://doi.org/10.1016/j.rser.2019.109548.
[6] K. Jacobson, K.C. Maheria, A. Kumar Dalai, Bio-oil valorization: a review, Renew. Sustain. Energy Rev. 23 (2013) 91–106, https://doi.org/10.1016/j.rser.2013.02.036.
[7] G.S. Foo, A.K. Rogers, M.M. Yung, C. Sievers, Steric effect and evolution of surface species in the hydrodeoxygenation of bio-oil model compounds over Pt/HBEA, ACS Catal. 6 (2016) 1292–1307, https://doi.org/10.1021/acscatal.5b02684.
[8] P.M. Mortensen, J.D. Grunwaldt, P.A. Jensen, A.D. Jensen, Screening of catalysts for hydrodeoxygenation of phenol as a model compound for bio-oil, ACS Catal. 3 (2013) 1774–1785, https://doi.org/10.1021/cs400266e.
[9] P. Yan, J. Mensah, M. Drewery, E. Kennedy, T. Maschmeyer, M. Stockenhuber, Role of metal support during ru-catalysed hydrodeoxygenation of biocrude oil, Appl. Catal. B Environ. 281 (2021), 119470, https://doi.org/10.1016/j.apcatb.2020.119470.
[10] B. Lin, R. Li, R. Shu, C. Wang, Z. Yuan, Y. Liu, Y. Chen, Synergistic effect of highly dispersed Ru and moderate acid site on the hydrodeoxygenation of phenolic compounds and raw bio-oil, J. Energy Inst. 93 (2020) 847–856, https://doi.org/10.1016/j.joei.2019.07.009.
[11] E.R. Naranov, K.I. Dement'ev, I.M. Gerzeliev, N.V. Kolesnichenko, E.A. Roldugina, A.L. Maksimov, The role of zeolite catalysis in modern petroleum refining: contribution from domestic technologies, Pet. Chem. 59 (2019) 247–261, https://doi.org/10.1134/S0965544119030101.
[12] C. Li, Y. Nakagawa, M. Tamura, A. Nakayama, K. Tomishige, Hydrodeoxygenation of guaiacol to phenol over ceria-supported iron catalysts, ACS Catal. 10 (2020) 14624–14639, https://doi.org/10.1021/acscatal.0c04336.
[13] C.E.J.J. Vriamont, T. Chen, C. Romain, P. Corbett, P. Manageracharath, J. Peet, C. M. Conifer, J.P. Hallett, G.J.P. Britovsek, From lignin to chemicals: hydrogenation of lignin models and mechanistic insights into hydrodeoxygenation via low-temperature C-O bond cleavage, ACS Catal. 9 (2019) 2345–2354, https://doi.org/10.1021/acscatal.8b04714.
[14] A. Kumar, B. Thallada, Hydrodeoxygenation of lignin derived phenolics over a hydrous ruthenium oxide based catalyst(s): role of surface water molecules and acidity of the support, Sustain. Energy Fuels. 5 (2021) 3802–3817, https://doi.org/10.1039/d1se00102g.
[15] E.A. Roldugina, E.R. Naranov, A.L. Maximov, E.A. Karakhanov, Hydrodeoxygenation of guaiacol as a model compound of bio-oil in methanol over mesoporous noble metal catalysts, Appl. Catal. A Gen. 553 (2018) 24–35, https://doi.org/10.1016/j.apcata.2018.01.008.
[16] W. Luo, W. Cao, P.C.A. Bruijnincx, L. Lin, A. Wang, T. Zhang, Zeolite-supported metal catalysts for selective hydrodeoxygenation of biomass-derived platform molecules, Green. Chem. 21 (2019) 3744–3768, https://doi.org/10.1039/c9gc01216h.
[17] M. Hua, J. Song, C. Xie, H. Wu, Y. Hu, X. Huang, B. Han, Ru/hydroxyapatite as a dual-functional catalyst for efficient transfer hydrogenolytic cleavage of aromatic ether bonds without additional bases, Green. Chem. 21 (2019) 5073–5079, https://doi.org/10.1039/c9gc02336d.
[18] M. Lu, H. Du, B. Wei, J. Zhu, M. Li, Y. Shan, J. Shen, C. Song, Hydrodeoxygenation of guaiacol on Ru catalysts: influence of TiO2-ZrO2 composite oxide supports, Ind. Eng. Chem. Res. 56 (2017) 12070–12079, https://doi.org/10.1021/acs.iecr.7b02569.
[19] F.N. Gu, F. Wei, J.Y. Yang, N. Lin, W.G. Lin, Y. Wang, J.H. Zhu, New strategy to synthesis of hierarchical mesoporous zeolites, Chem. Mater. 22 (2010) 2442–2450, https://doi.org/10.1021/cm903785r.
[20] J. Pérez-Ramírez, C.H. Christensen, K. Egeblad, C.H. Christensen, J.C. Groen, Hierarchical zeolites: enhanced utilisation of microporous crystals in catalysis by advances in materials design, Chem. Soc. Rev. 37 (2008) 2530, https://doi.org/10.1039/b809030k.
[21] R. Ryoo, K. Cho, F.M. Mota, Mesostructured Zeolites, in: Zeolites Sustain. Chem. Synth. Charact. Catal. Appl., Springer Berlin Heidelberg, 2016, pp. 101–148, https://doi.org/10.1007/978-3-662-47395-5_4.
[22] K. Na, M. Choi, R. Ryoo, Recent advances in the synthesis of hierarchically nanoporous zeolites, Microporous Mesoporous Mater. 166 (2013) 3–19, https://doi.org/10.1016/j.micromeso.2012.03.054.
[23] Q. Tang, H. Xu, Y. Zheng, J. Wang, H. Li, J. Zhang, Catalytic dehydration of methanol to dimethyl ether over micro – mesoporous ZSM - 5 / MCM - 41 composite molecular sieves, Appl. Catal. A Gen. (2012) 413–414, https://doi.org/10.1016/j.apcata.2011.10.039.
[24] E.A. Roldugina, A.P. Glotov, A.L. Isakov, A.L. Maksimov, V.A. Vinokurov, E. A. Karakhanov, Ruthenium catalysts on ZSM-5/MCM-41 micro-mesoporous support for hydrodeoxygenation of guaiacol in the presence of water, Russ. J. Appl. Chem. 92 (2019) 1170–1178, https://doi.org/10.1134/S1070427219080172.
[25] M. Rutkowska, L. Chmielarz, D. Macina, Z. Piwowarska, B. Dudek, a. Adamski, S. Witkowski, Z. Sojka, L. Obalová, C.J. Van Oers, P. Cool, Catalytic decomposition and reduction of N2O over micro-mesoporous materials containing Beta zeolite nanoparticles, Appl. Catal. B Environ. 146 (2014) 112–122, https://doi.org/10.1016/j.apcatb.2013.05.005.
[26] M. Shamzhy, B. Gil, M. Opanasenko, W.J. Roth, J. Čejka, MWW and MFI frameworks as model layered zeolites: structures, transformations, properties, and activity, ACS Catal. 11 (2021) 2366–2396, https://doi.org/10.1021/acscatal.0c05332.
[27] G. Jiang, Y. Hu, G. Xu, X. Mu, H. Liu, Controlled hydrodeoxygenation of phenolic components in pyrolysis bio-oil to arenes, ACS Sustain. Chem. Eng. 6 (2018) 5772–5783, https://doi.org/10.1021/acssuschemeng.7b03276.
[28] Z. Luo, Y. Wang, M. He, C. Zhao, Precise oxygen scission of lignin derived aryl ethers to quantitatively produce aromatic hydrocarbons in water, Green. Chem. 18 (2016) 433–441, https://doi.org/10.1039/c5gc01790d.
[29] Y. Seo, K. Cho, Y. Jung, R. Ryoo, Characterization of the surface acidity of MFI zeolite nanosheets by 31 P NMR of adsorbed phosphine oxides and catalytic cracking of decalin, ACS Catal. 3 (2013) 713–720, https://doi.org/10.1021/cs300824e.
[30] K. Na, C. Jo, J. Kim, K. Cho, J. Jung, Y. Seo, R.J. Messinger, B.F. Chmelka, R. Ryoo, Directing zeolite structures into hierarchically nanoporous architectures, Sci. (80-.). 333 ((2011) 328–332, https://doi.org/10.1126/science.1204452.
[31] E.R. Naranov, A.A. Sadovnikov, A.L. Bugaev, D.A. Shavaleev, A.L. Maximov, A stepwise fabrication of MFI nanosheets in accelerated mode, Catal. Today 378 (2021) 149–157, https://doi.org/10.1016/j.cattod.2021.06.011.
[32] E.R. Naranov, A.A. Sadovnikov, I.M. Vatsouro, A.L. Maximov, The mechanism of promoter-induced zeolite nanosheet crystallization under hydrothermal and microwave irradiation conditions, Inorg. Chem. Front. 7 (2020) 1400–1410, https://doi.org/10.1039/d0qi00012d.
[33] S. Salakhum, T. Yutthalekha, M. Chareonpanich, J. Limtrakul, C. Wattanakit, Synthesis of hierarchical faujasite nanosheets from corn cob ash-derived nanosilica as efficient catalysts for hydrogenation of lignin-derived alkylphenols, Microporous Mesoporous Mater. 258 (2018) 141–150, https://doi.org/10.1016/j.micromeso.2017.09.009.
[34] L. Chen, X. Ma, F. Tang, Y. Li, Z. Yu, X. Chen, Comparison of catalytic effect on upgrading bio-oil derived from co-pyrolysis of water hyacinth and scrap tire over multilamellar MFI nanosheets and HZSM-5, Bioresour. Technol. 312 (2020), 123592, https://doi.org/10.1016/j.biortech.2020.123592.
[35] H.W. Lee, S.H. Park, J.K. Jeon, R. Ryoo, W. Kim, D.J. Suh, Y.K. Park, Upgrading of bio-oil derived from biomass constituents over hierarchical unilamellar mesoporous MFI nanosheets, in: Catal. Today, Elsevier, 2014, pp. 119–126, https://doi.org/10.1016/j.cattod.2013.12.015.
[36] A.H. Zacher, M.V. Olarte, D.M. Santosa, D.C. Elliott, S.B. Jones, A review and perspective of recent bio-oil hydrotreating research, Green. Chem. 16 (2014) 491–515, https://doi.org/10.1039/c3gc41382a.
[37] Q. Wang, S. Santos, C.A. Urbina-Blanco, W. Zhou, Y. Yang, M. Marinova, S. Heyte, T.R. Joelle, O. Ersen, W. Baaziz, O.V. Safonova, M. Saeys, V.V. Ordomsky, Ru(III) single site solid micellar catalyst for selective aqueous phase hydrogenation of carbonyl groups in biomass-derived compounds, Appl. Catal. B Environ. 300 (2022), https://doi.org/10.1016/j.apcatb.2021.120730.
[38] C.R. Lee, J.S. Yoon, Y.W. Suh, J.W. Choi, J.M. Ha, D.J. Suh, Y.K. Park, Catalytic roles of metals and supports on hydrodeoxygenation of lignin monomer guaiacol, Catal. Commun. 17 (2012) 54–58, https://doi.org/10.1016/j.catcom.2011.10.011.
[39] C.A. Teles, P.M. de Souza, R.C. Rabelo-Neto, A. Teran, G. Jacobs, C. Vilela Weikert, Z.M. Magriotis, V.O.O. Gonçalves, D.E. Resasco, F.B. Noronha, Reaction pathways for the HDO of guaiacol over supported Pd catalysts: effect of support type in the deoxygenation of hydroxyl and methoxy groups, Mol. Catal. 523 (2022), 111491, https://doi.org/10.1016/j.mcat.2021.111491.
[40] Q. Tan, G. Wang, A. Long, A. Dinse, C. Buda, J. Shabaker, D.E. Resasco, Mechanistic analysis of the role of metal oxophilicity in the hydrodeoxygenation of anisole, J. Catal. 347 (2017) 102–115, https://doi.org/10.1016/j.jcat.2017.01.008.
[41] A. Bjelić, M. Grilc, M. Huš, B. Likozar, Hydrogenation and hydrodeoxygenation of aromatic lignin monomers over Cu/C, Ni/C, Pd/C, Pt/C, Rh/C and Ru/C catalysts: mechanisms, reaction micro-kinetic modelling and quantitative structure-activity relationships, Chem. Eng. J. 359 (2019) 305–320, https://doi.org/10.1016/j.cej.2018.11.107.
[42] A. Kumar, A. Kumar, B. Biswas, J. Kumar, S.R. Yenumala, T. Bhaskar, Hydrodeoxygenation of m-Cresol over Ru based catalysts: influence of catalyst support on m-cresol conversion and methylcyclohexane selectivity, Renew. Energy 151 (2020) 687–697, https://doi.org/10.1016/j.renene.2019.11.076.
[43] Z. Zheng, Z. Luo, C. Zhao, Morphologically cross-shaped Ru/HZSM-5 catalyzes tandem hydrogenolysis of guaiacol to benzene in water, ChemCatChem 10 (2018) 1376–1384, https://doi.org/10.1002/cctc.201701398.
[44] J. Shangguan, A.J.R. Hensley, M.V. Gradiski, N. Pfriem, J.S. McEwen, R.H. Morris, Y.H.C. Chin, The role of protons and hydrides in the catalytic hydrogenolysis of guaiacol at the ruthenium nanoparticle-water interface, ACS Catal. 10 (2020) 12310–12332, https://doi.org/10.1021/acscatal.0c01963.
[45] R. Insyani, A.F. Barus, R. Gunawan, J. Park, G.T. Jaya, H.S. Cahyadi, M.G. Sibi, S. K. Kwak, D. Verma, J. Kim, RuO2–Ru/Hβ zeolite catalyst for high-yield direct conversion of xylose to tetrahydrofurfuryl alcohol, Appl. Catal. B Environ. 291 (2021), https://doi.org/10.1016/j.apcatb.2021.120120.
[46] J. Cha, T. Lee, Y.-J. Lee, H. Jeong, Y.S. Jo, Y. Kim, S.W. Nam, J. Han, K.B. Lee, C. W. Yoon, H. Sohn, Highly monodisperse sub-nanometer and nanometer Ru particles confined in alkali-exchanged zeolite Y for ammonia decomposition, Appl. Catal. B Environ. 283 (2021), 119627, https://doi.org/10.1016/j.apcatb.2020.119627.
[47] S. Gundekari, K. Srinivasan, Hydrous ruthenium oxide: A new generation remarkable catalyst precursor for energy efficient and sustainable production of Γ-valerolactone from levulinic acid in aqueous medium, Appl. Catal. A Gen. 569 (2019) 117–125, https://doi.org/10.1016/j.apcata.2018.10.018.
[48] J.L. Gómez de la Fuente, M.V. Martínez-Huerta, S. Rojas, P. Hernández-Fernández, P. Terreros, J.L.G. Fierro, M.A. Peña, Tailoring and structure of PtRu nanoparticles supported on functionalized carbon for DMFC applications: New evidence of the hydrous ruthenium oxide phase, Appl. Catal. B Environ. 88 (2009) 505–514, https://doi.org/10.1016/j.apcatb.2008.10.016.
[49] P.V. Shvets, P.A. Prokopovich, A.I. Dolgoborodov, O.A. Usoltsev, A.A. Skorynina, E.G. Kozyr, V.V. Shapovalov, A.A. Guda, A.L. Bugaev, E.R. Naranov, D.

N. Gorbunov, K. Janssens, D.E. De Vos, A.L. Trigub, E. Fonda, M.B. Leshchinsky, V. R. Zagackij, A.V. Soldatov, A.Y. Goikhman, In Situ x-ray absorption spectroscopy cells for high pressure homogeneous catalysis, Catalysts 12 (2022) 1264, https://doi.org/10.3390/catal12101264.
[50] Y. Han, A.P. Pinheiro Pires, M. Denson, A.G. McDonald, M. Garcia-Perez, Ternary phase diagram of water/bio-oil/organic solvent for bio-oil fractionation, Energy Fuels. 34 (2020) 16250–16264, https://doi.org/10.1021/acs.energyfuels.0c03100.
[51] M. Kruk, M. Jaroniec, Y. Sakamoto, O. Terasaki, R. Ryoo, C.H. Ko, Determination of pore size and pore wall structure of MCM-41 by using nitrogen adsorption, transmission electron microscopy, and x-ray diffraction, J. Phys. Chem. B. 104 (2000) 292–301, https://doi.org/10.1021/jp992718a.
[52] H.A.G. Gasteiger, J. Garche, Handbook of Heterogeneous Catalysis, 2008. https://www.wiley.com/en-us/Handbook+of+Heterogeneous+Catalysis%2C+8+Volume+Set%2C+2nd+Edition-p-9783527312412 (accessed April 14, 2023).
[53] M. Tamura, K. Shimizu, A. Satsuma, Comprehensive IR study on acid/base properties of metal oxides, Appl. Catal. A Gen. 433–434 (2012) 135–145, https://doi.org/10.1016/j.apcata.2012.05.008.
[54] J.P. Perdew, Accurate density functional for the energy: real-space cutoff of the gradient expansion for the exchange hole, Phys. Rev. Lett. 55 (1985) 1665–1668, https://doi.org/10.1103/PhysRevLett.55.1665.
[55] G. Kresse, J. Furthmüller, Efficient iterative schemes for ab initio total-energy calculations using a plane-wave basis set, Phys. Rev. B - Condens. Matter Mater. Phys. 54 (1996) 11169–11186, https://doi.org/10.1103/PhysRevB.54.11169.
[56] G. Kresse, J. Furthmüller, Efficiency of ab-initio total energy calculations for metals and semiconductors using a plane-wave basis set, Comput. Mater. Sci. 6 (1996) 15–50, https://doi.org/10.1016/0927-0256(96)00008-0.
[57] A. Martini, S.A. Guda, A.A. Guda, G. Smolentsev, A. Algasov, O. Usoltsev, M. A. Soldatov, A. Bugaev, Y. Rusalev, C. Lamberti, A.V. Soldatov, PyFitit: the software for quantitative analysis of XANES spectra using machine-learning algorithms, Comput. Phys. Commun. 250 (2020), 107064, https://doi.org/10.1016/j.cpc.2019.107064.
[58] C.H. Camp, PyMCR: a python library for multivariatecurve resolution analysis with alternating regression (MCR-AR), J. Res. Natl. Inst. Stand. Technol. 124 (2019) 1, https://doi.org/10.6028/jres.124.018.
[59] G. French, The Larch Environment - Python programs as visual, interactive literature, (2013). https://ueaeprints.uea.ac.uk/42343/1/2013FrenchGWMSc.pdf (accessed May 10, 2022).
[60] A.A. Sadovnikov, O.V. Arapova, V. Russo, A.L. Maximov, D.Y. Murzin, Synergy of acidity and morphology of micro-/mesoporous materials in the solid-acid alkylation of toluene with 1-decene, Ind. Eng. Chem. Res. 61 (2022) 1994–2009, https://doi.org/10.1021/acs.iecr.1c04169.
[61] S.H. Lee, P. Liu, H.M. Cheong, C. Edwin Trecy, S.K. Deb, Electrochromism of amorphous ruthenium oxide thin films, in: Solid State Ionics, Elsevier, 2003, pp. 217–221, https://doi.org/10.1016/j.ssi.2003.08.035.
[62] R. Inguanta, G. Ferrara, P. Livreri, S. Piazza, C. Sunseri, Ruthenium oxide nanotubes via template electrosynthesis, Curr. Nanosci. 7 (2011) 210–218, https://doi.org/10.2174/157341311794653622.
[63] N. Perkas, Z. Zhong, L. Chen, M. Besson, A. Gedanken, Sonochemically prepared high dispersed Ru/TiO2 mesoporous catalyst for partial oxidation of methane to syngas, Catal. Lett. 103 (2005) 9–14, https://doi.org/10.1007/s10562-005-6496-4.
[64] D. Duraczyńska, A. Michalik-Zym, B.D. Napruszewska, R. Dula, R.P. Socha, L. Lityńska-Dobrzyńska, A. Gaweł, K. Bahranowski, E.M. Serwicka, Efficient and versatile Ru/SBA-15 catalysts for liquid-phase hydrogenation of the C⁻⁻C and C⁻⁻O bonds under mild conditions, ChemistrySelect 1 (2016) 2148–2155, https://doi.org/10.1002/slct.201600491.
[65] K.L. Deutsch, B.H. Shanks, Hydrodeoxygenation of lignin model compounds over a copper chromite catalyst, Appl. Catal. A Gen. 447–448 (2012) 144–150, https://doi.org/10.1016/j.apcata.2012.09.047.
[66] M. Saleheen, A.M. Verma, O. Mamun, J. Lu, A. Heyden, Investigation of solvent effects on the hydrodeoxygenation of guaiacol over Ru catalysts, Catal. Sci. Technol. 9 (2019) 6253–6273, https://doi.org/10.1039/c9cy01763a.
[67] C.C. Chiu, A. Genest, A. Borgna, N. Rösch, Hydrodeoxygenation of guaiacol over Ru(0001): a DFT study, ACS Catal. 4 (2014) 4178–4188, https://doi.org/10.1021/cs500911j.
[68] A.A. Dwiatmoko, I. Kim, L. Zhou, J.W. Choi, D.J. Suh, J. Jae, J.M. Ha, Hydrodeoxygenation of guaiacol on tungstated zirconia supported Ru catalysts, Appl. Catal. A Gen. 543 (2017) 10–16, https://doi.org/10.1016/j.apcata.2017.05.037.
[69] R. Tu, W. Lv, Y. Sun, Y. Wu, Y. Wu, X. Fan, E. Jiang, Q. Lu, X. Xu, Ru-RuO2–Nb2O5/Hβ zeolite catalyst for high-active hydrogenation of lignin derivatives at room temperature, Chem. Eng. J. 453 (2023), 139718, https://doi.org/10.1016/j.cej.2022.139718.
[70] A. Sulman, P. Mäki-Arvela, L. Bomont, M. Alda-Onggar, V. Fedorov, V. Russo, K. Eränen, M. Peurla, U. Akhmetzyanova, L. Skuhrovcová, Z. Tišler, H. Grénman, J. Wärnå, D.Y. Murzin, Kinetic and thermodynamic analysis of guaiacol hydrodeoxygenation, Catal. Lett. 149 (2019) 2453–2467, https://doi.org/10.1007/s10562-019-02856-x.
[71] M. Ishikawa, M. Tamura, Y. Nakagawa, K. Tomishige, Demethoxylation of guaiacol and methoxybenzenes over carbon-supported Ru–Mn catalyst, Appl. Catal. B Environ. 182 (2016) 193–203, https://doi.org/10.1016/j.apcatb.2015.09.021.
[72] E. Furimsky, Catalytic hydrodeoxygenation, Appl. Catal. A Gen. 199 (2000) 147–190, https://doi.org/10.1016/S0926-860X(99)00555-4.
[73] P.M. de Souza, R.C. Rabelo-Neto, L.E.P. Borges, G. Jacobs, B.H. Davis, T. Sooknoi, D.E. Resasco, F.B. Noronha, Role of keto intermediates in the hydrodeoxygenation of phenol over Pd on oxophilic supports, ACS Catal. 5 (2015) 1318–1329, https://doi.org/10.1021/cs501853t.
[74] T. Förster, Chemical Applications of Spectroscopy, von W. West. (Technique of Organic Chemistry, Vol. IX. Herausgeber A. Weissberger). Interscience Publishers, New York 1956. 1. Aufl., XXIV, 787 S., geb. $ 15. —, John Wiley & Sons, Ltd, 1957. https://doi.org/10.1002/ANGE.19570692219.
[75] V. Fridman, Dehydrogenation of cyclohexanol on copper-containing catalysts II. The pathways of the cyclohexanol dehydrogenation reaction to cyclohexanone on copper-active sites in oxidation state Cu0 and Cu, J. Catal. 222 (2004) 545–557, https://doi.org/10.1016/j.jcat.2003.12.016.
[76] D.S. Zijlstra, A. De Santi, B. Oldenburger, J. De Vries, K. Barta, P.J. Deuss, Extraction of lignin with high β-O-4 content by mild ethanol extraction and its effect on the depolymerization yield, J. Vis. Exp. 2019 (2019) 58575, https://doi.org/10.3791/58575.
[77] E. Jasiukaitytė-Grojzdek, M. Huš, M. Grilc, B. Likozar, Acid-catalyzed α-O-4 aryl-ether cleavage mechanisms in (Aqueous) γ-valerolactone: catalytic depolymerization reactions of lignin model compound during organosolv pretreatment, ACS Sustain. Chem. Eng. 8 (2020) 17475–17486, https://doi.org/10.1021/ACSSUSCHEMENG.0C06099/ASSET/IMAGES/LARGE/SC0C06099_0008.JPEG.
[78] C. Crestini, H. Lange, M. Sette, D.S. Argyropoulos, On the structure of softwood kraft lignin, Green. Chem. 19 (2017) 4104–4121, https://doi.org/10.1039/C7GC01812F.
[79] C. Iwakura, M. Tanaka, S. Nakamatsu, H. Inoue, M. Matsuoka, N. Furukawa, Electrochemical properties of Ni (Ni + RuO2) active cathodes for hydrogen evolution in chlor-alkali electrolysis, Electrochim. Acta 40 (1995) 977–982, https://doi.org/10.1016/0013-4686(95)00006-Z.
[80] E.R. Naranov, A.A. Sadovnikov, O.V. Arapova, A.L. Bugaev, O.A. Usoltsev, D. N. Gorbunov, V. Russo, D.Y. Murzin, A.L. Maximov, Mechanistic insights on Ru nanoparticle in situ formation during hydrodeoxygenation of lignin-derived substances to hydrocarbons, Catal. Sci. Technol. 13 (2023) 1571–1583, https://doi.org/10.1039/D2CY01127A.
[81] M. Huš, A. Bjelić, M. Grilc, B. Likozar, First-principles mechanistic study of ring hydrogenation and deoxygenation reactions of eugenol over Ru(0001) catalysts, J. Catal. 358 (2018) 8–18, https://doi.org/10.1016/j.jcat.2017.11.020.